Petroleum Science 22 (2025) 4117–4133

Contents lists available at ScienceDirect

Petroleum Science

journal homepage: www.keaipublishing.com/en/journals/petroleum-science

Study on the synergistic effects of dynamic impact damage and acid etching treatment on the mechanical properties and pore characteristics of shale

Mao Jing, Kang Peng *, Tao Wu, Han-Kuo Zhang, Si-Yu Gao

School of Resources and Safety Engineering, Central South University, Changsha, 410083, Hunan, China

ARTICLE INFO

Article history:
Received 13 January 2025
Received in revised form
15 July 2025
Accepted 18 July 2025
Available online 28 July 2025

Edited by Jia-Jia Fei

Keywords:
Shale
Acid etching
Combined damage
Mechanical properties
Microstructure

ABSTRACT

The low porosity and low permeability of shale remain the primary challenges in shale gas exploitation. Traditional single permeability enhancement techniques have shown limited efficacy, failing to effectively address these technical bottlenecks. This study investigates the synergistic effects of perforation-induced permeability enhancement and acidizing operations on the mechanical properties and micropore structure of shale. The improved Split Hopkinson Pressure Bar (SHPB) technique was employed to simulate dynamic impact damage under triaxial stress conditions. Damaged and undamaged rock specimens were immersed in a 15% hydrochloric acid solution to fabricate combined-damage specimens and acid-etched specimens with varying damage states. Uniaxial compression tests, X-ray diffraction (XRD) analysis, and scanning electron microscopy (SEM) were conducted on these specimens. SEM images were binarized, and combined with low-temperature nitrogen adsorption tests, the effects of different damage states on the mechanical behavior, energy dissipation, micro-morphology, and pore characteristics of shale were systematically evaluated. Results demonstrate that the peak stress and elastic modulus of shale exhibit a negative correlation with acid-etching duration. The mechanical properties of combined-damage specimens are inferior to those of pure acid-etched specimens, with the minimum peak stress reaching 147.10 MPa—a 43.53% reduction compared to untreated specimens. The energy dissipation ratio significantly increases, with a maximum value of 34.74%. XRD analysis reveals that prolonged acid immersion effectively reduces the carbonate content in specimens, while composite treatment accelerates the reaction between rock matrix and acid solution. Microstructural characterization indicates that acid etching enhances the porosity of shale, particularly the area of mesopores and macropores, with more pronounced pore development and a fragmented interface structure. These findings deepen the understanding of physical mechanisms during shale gas extraction and provide critical theoretical support for optimizing integrated permeability enhancement technologies.

1. Introduction

Shale gas, an unconventional natural gas resource stored in shale matrix and micro-nano pores, plays a strategic role in modern energy transition (Li et al., 2025a, b; Cheng et al., 2024a, b). However, its exploitation faces significant challenges, primarily due to the generally low porosity and permeability of shale reservoirs, which lead to relatively high formation fracturing pressures and complicate extraction (Zhao et al., 2024; Wei et al., 2021; Huang et al., 2024a, b). To address this, the engineering sector has innovatively combined perforation technology with acidizing treatment, forming a synergistic perforation-acidizing composite process (Xiao et al., 2024; Cheng et al., 2024a,b). This process first uses a shaped charge perforation device to fracture the gas-bearing formation, causing structural damage to the shale reservoir, followed by acid injection to dissolve internal minerals and remove substances hindering fluid flow (Fig. 1). This combined action significantly enhances structural defects and mechanical damage characteristics of shale, thereby improving its permeability and boosting shale gas recovery efficiency (Chang et al., 2024; Sheng et al., 2021; Wang et al., 2024).

* Corresponding author.
E-mail address: pengkang2020@csu.edu.cn (K. Peng).
Peer review under the responsibility of China University of Petroleum (Beijing).

https://doi.org/10.1016/j.petsci.2025.07.011

Extensive research on acid treatment of shale has been conducted by scholars at home and abroad (Wang et al., 2023; Xu et al., 2024). Studies have shown that when treating shale with low-concentration hydrochloric acid (1–3 wt%), the porosity significantly increases after treatment with 3 wt% hydrochloric acid for 3 h (Morsy et al., 2013). High-concentration hydrochloric acid (15%) can optimize pore connectivity and enhance fluidity (Cash et al., 2016). Although existing research has emphasized the positive effects of acid treatment on improving porosity and conductivity, there is still a lack of systematic exploration of its comprehensive impacts on other physical and mechanical properties. To gain in-depth understanding of the mechanism of acid treatment, XRD and SEM were used to analyze the mineral composition and microstructural changes of acid-soaked shale. It was found that high-concentration hydrochloric acid significantly alters shale through dissolution, forming pores and affecting permeability (Grieser et al., 2007). Uniaxial compression tests, triaxial hydraulic fracturing simulations, nuclear magnetic resonance, and other methods were employed to study the effects of hydrochloric acid on the mechanical properties and permeability of rock samples. The results showed that acid etching reduces the mechanical properties of rock samples, promotes the development of pores and fractures, and improves permeability (Teklu et al., 2017; Tan et al., 2018). However, the quantitative influence of acid concentration and treatment time on permeability remains unclear, limiting its engineering applications. Mixed acid solutions have significant effects on the mechanical properties, microstructure, and pore structure of shale (Adnan et al., 2009; Wang et al., 2023; Zhang et al., 2023). For example, mixed acids (hydrochloric acid and hydrofluoric acid) can reduce the compressive strength and elastic modulus of rock samples, making them more fragile, alter the microstructure by dissolving mineral components, and enhance the pore structure (Chen et al., 2019). In addition, high-concentration hydrochloric acid (15%) significantly enhances the pore connectivity of shale and improves conductivity (Cash et al., 2016), and the optimal injection rate is 2 cm^3/min (Li et al., 2020), providing support for the application of acidization enhancement technology in shale gas development.

Previous research has primarily focused on the effects of acid treatment alone (Wang et al., 2023). However, actual shale gas extraction often employs multiple synergistic permeability enhancement methods to more effectively improve shale permeability. Perforation-acidizing collaborative operation is a commonly used composite technology. In this process, operators first perform physical fracturing using perforating guns, followed by acid injection for enhanced permeability. To simulate perforation fracturing under triaxial stress, this study used a triaxial dynamic impact testing system to prepare dynamically damaged rock samples. Damaged and undamaged samples were then immersed in 15% hydrochloric acid solution for different durations to fabricate combined-damage and acid-etched samples, simulating the rock state under synergistic perforation-acidizing. Finally, uniaxial compression tests, XRD, and SEM were conducted on samples with different damage states to systematically investigate the effects on mechanical properties, energy dissipation, micro-morphology, and pore characteristics.

2. Experimental materials and methods

2.1. Selection and preparation of samples

The shale used in this study was sourced from the Wufeng Formation of the Ordovician period and the Longmaxi Formation of the Silurian period, located in Changning County, Sichuan Province, China. X-ray diffraction tests were performed to determine the mineral composition and their respective contents in the rock samples, as illustrated in Fig. 2(a). The composition was found to be as follows: quartz 57.15%, dolomite 9.14%, calcite 16.5%, pyrite 0.93%, and iron dolomite 9.14%, with other components constituting 7.14%. Notably, quartz, dolomite, and calcite comprised a significant portion of the total mineral composition, totaling 82.79% (Fig. 2(b)).

Multiple cylindrical samples, each measuring Ø50 mm × 50 mm, were prepared from vertical stratified layers, and the surfaces of these samples were polished. Samples exhibiting visible cracks or damage on their surfaces were discarded. Vaseline was evenly applied to the bottom surfaces of the samples. Each sample's longitudinal wave velocity was individually tested using the HS-YS4A rock acoustic parameter tester, with outlier samples being excluded from further analysis.

2.2. SHPB dynamic impact experiment

To simulate perforation fracturing operations under three-dimensional stress conditions, dynamic impact damage tests were conducted on shale samples using the SHPB testing system under triaxial compression. The confining pressure and axial pressure of the impact testing device were both set to 10 MPa. Dynamic impact experiments were then performed on the shale samples at three different impact gas pressures: 0.6, 0.8, and 1.0 MPa. The results indicated that the shale did not experience overall failure at 0.6 MPa, while micro-damage was observed on the surface of the shale at 0.8 MPa. At 1.0 MPa, the sample fractured along its vertical layering. Consequently, dynamic impact damage tests on shale were conducted at an impact gas pressure of 0.8 MPa. Therefore, under the three-dimensional stress state with both confining pressure and axial pressure set to 10 MPa, an impact gas pressure of 0.8 MPa was chosen for the dynamic impact damage tests on shale, resulting in the preparation of the impacted damage sample S-Blank. The impacted damage samples and undamaged samples (Blank) are reserved for future acid etching tests and performance detection experiments.

2.3. Acid etching experiment

A series of hydrochloric acid solutions with a concentration of 15% were prepared from a standard 20% hydrochloric acid solution and distilled water. These solutions were stored in polytetrafluoroethylene beakers. Five groups of undamaged shale samples and five groups of damaged shale samples were systematically immersed in the hydrochloric acid solution to undergo acid etching experiments for five different durations: 1, 3, 7, 14, and 28 d. This resulted in the preparation of single acid-etched shale samples (A1d, A3d, A7d, A14d, and A28d) and combined damaged shale samples (SA1d, SA3d, SA7d, SA14d, and SA28d). After the acid etching experiments were completed, the shale samples were rinsed in deionized water for dilution. Subsequently, the samples were placed in a hot air convection oven at 100 °C for 24 h to dry and were then set aside for further use.

2.4. pH value detection of residual acid

The residual acid in the eroded shale samples was analyzed for pH. The pH value of the soaking solution was measured using a Leici PHS-3C pH meter manufactured by Shanghai Instrumentation Electric Science Co., Ltd., which has a minimum resolution of 1 mV, a pH range of −2.00 to 18.00, and a minimum resolution of 0.01 pH.

2.5. Static uniaxial compression experiment

A static uniaxial compression test was conducted using the INSTRON-1346 electro-hydraulic servo universal testing machine,

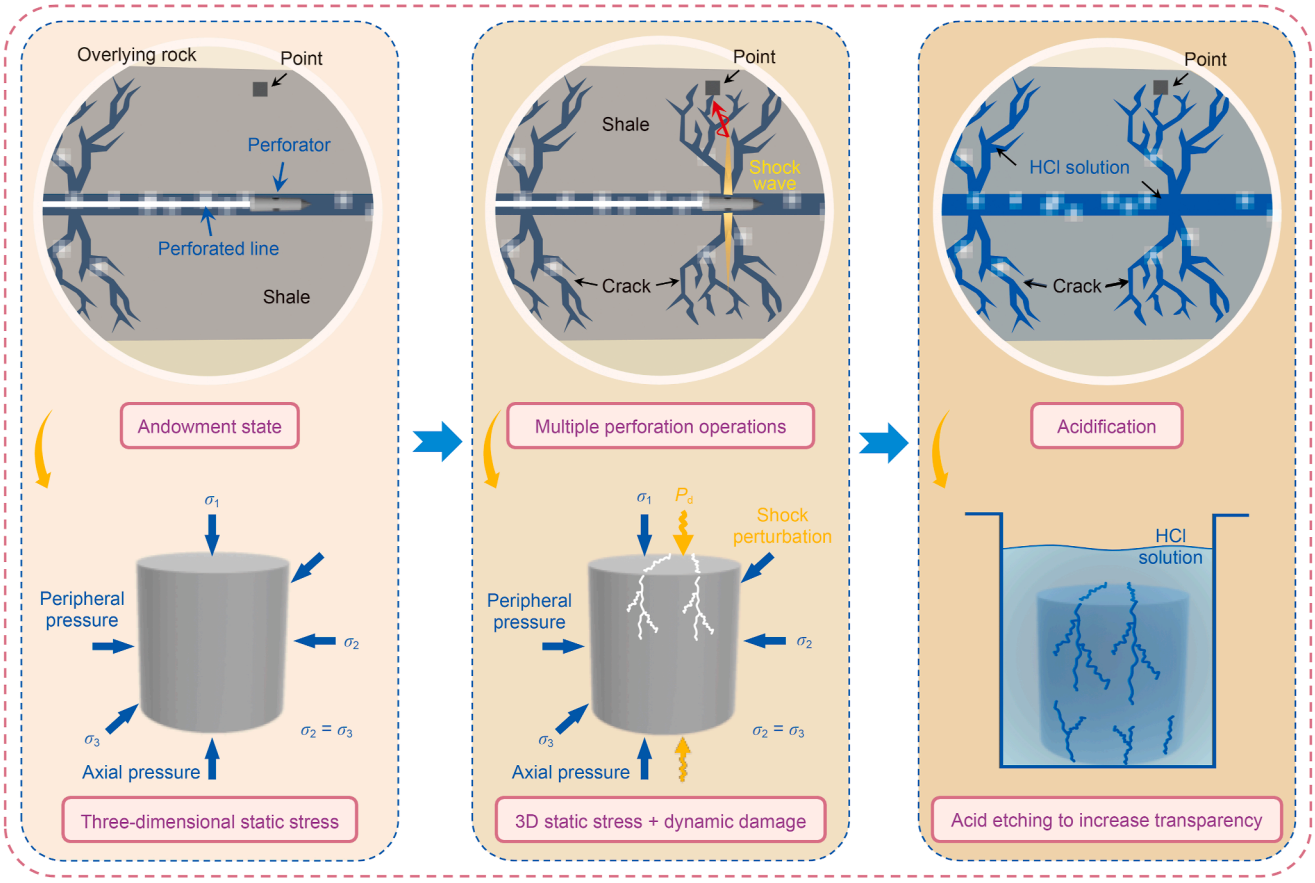

Fig. 1. Schematic diagram of shale shot hole acidizing and penetration enhancement operation.

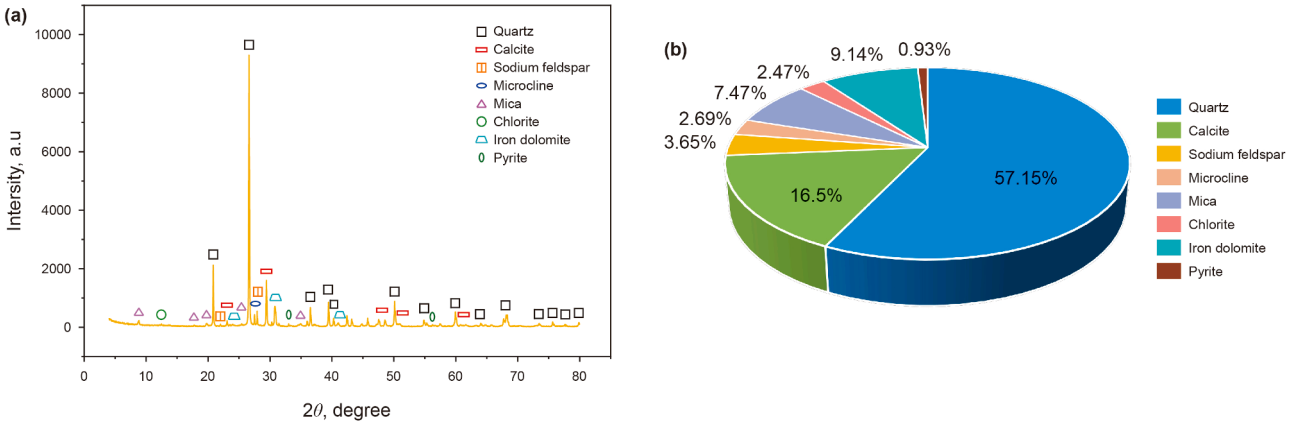

Fig. 2. XRD test results of shale and mineral composition analysis.

manufactured by Interstrand in the UK. During the test, an axial load was applied to the samples at a loading rate of 0.5 mm/min until failure occurred. Three samples were prepared for each damage state of shale, and one sample close to the average value was selected for mechanical performance analysis. Fig. 3 illustrates the preparation and experimental process of the damaged rock samples.

2.6. XRD

The materials were characterized using XRD with a powder diffractometer (Model D8, Advance). Samples with a particle size of 200 mesh or finer were selected for the tests, with approximately 0.5 g of sample powder used for each measurement. The scanning range was set from 5° to 80°, and the scanning speed was 5 °/min.

2.7. SEM

In this study, a Quanta 250 scanning electron microscope produced by TESCAN Brno, s.r.o., was used to observe the microstructure of the shale. The main parameters of the equipment were set at 30 kV, with a resolution of 1 nm at 1 kV and 3.5 nm at 30 kV. Rock samples were processed into thin sections with a diameter of less than 0.5 cm for experimental observation.

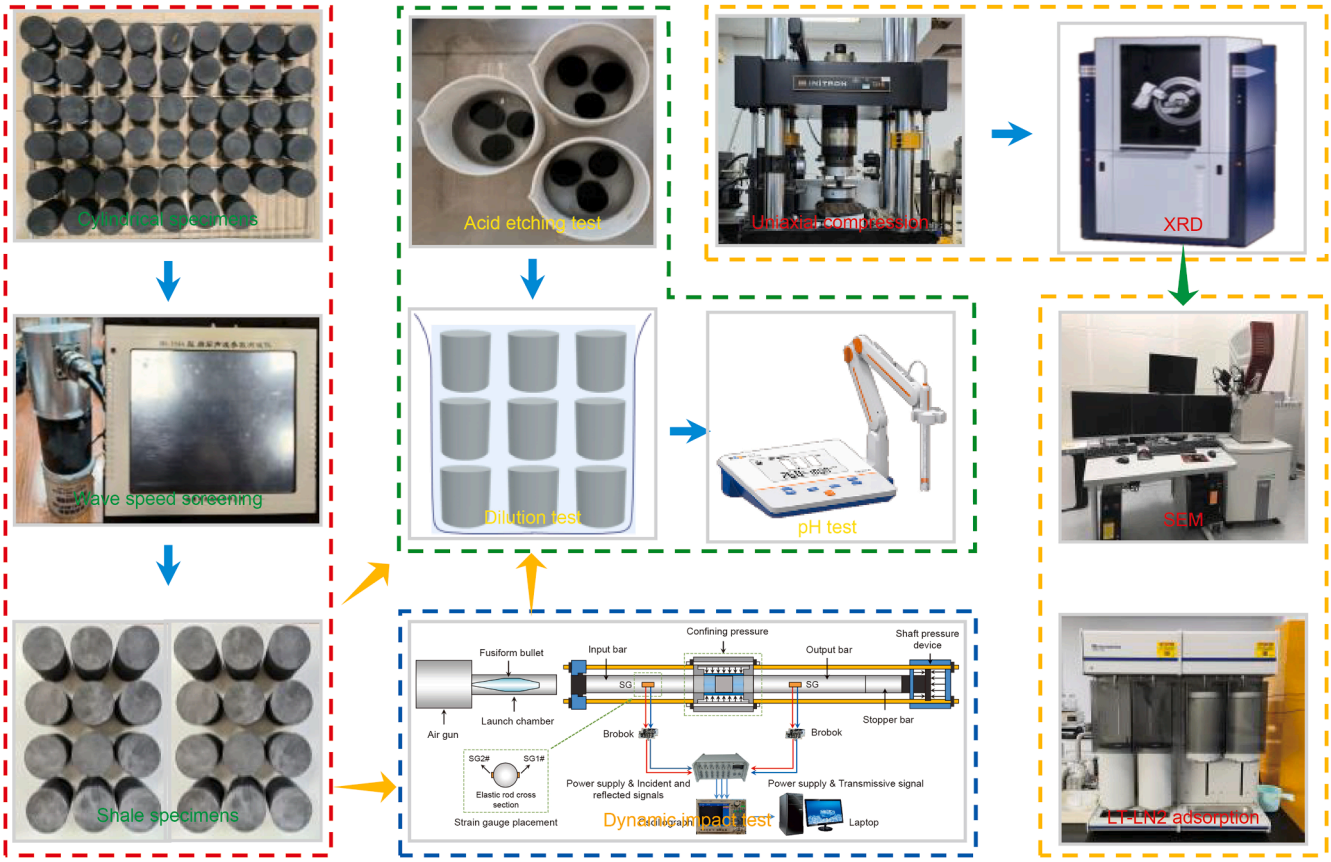

Fig. 3. Preparation and experimental flow chart of damaged rock samples.

2.8. Low-temperature nitrogen adsorption experiment

An ASAP-2460 automatic surface area and porosity analyzer was employed to test the samples, generating the isothermal adsorption curves of the rock samples. For the experiments, particles sized 60–80 mesh were selected, with approximately 2 g of sample placed in the sample tube. The samples were subjected to vacuum degassing for 10 h in a degassing station. Finally, the rock samples were placed in the apparatus for the liquid nitrogen adsorption experiment.

3. Experimental results and analysis

3.1. pH value detection results of residual acid

Fig. 4 shows the pH value changes of residual solutions after 15% hydrochloric acid etching of shale under 1, 3, 7, 14, and 28 d conditions. The results indicate that the pH value of the acid solution generally increases gradually with the extension of etching time. The residual solution after 1 d etching treatment has the highest pH growth rate, suggesting that hydrochloric acid reacts rapidly with shale upon contact, leading to a sharp increase in pH value. However, after 3, 7, 14, and 28 d treatments, the pH growth rate gradually slows down, indicating that the reaction between hydrochloric acid and shale tends to reach saturation with prolonged reaction time. In addition, the pH value of the acid immersion solution for composite-treated shale is significantly higher than that for single acid-etched shale, further demonstrating that composite treatment can more effectively promote the interaction between acid and shale and improve the efficiency of acid-rock reactions.

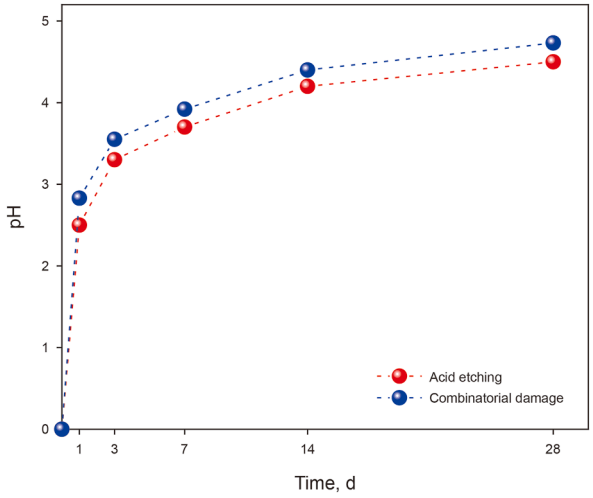

Fig. 4. pH value detection of residual acid.

3.2. Influence on mechanical properties

The stress-strain curve is a critical indicator for evaluating material elasticity, yield behavior, and ultimate strength (Hu et al., 2023; Jing et al., 2022). Static uniaxial compression tests were conducted to plot the stress-strain curves of 12 groups of rock samples with different damage states (Fig. 5), which can be divided into four stages: OA, AB, BC, and post-point C (Liu et al., 2024a, b; Ni et al., 2024). The OA stage is the compaction phase,

where internal micro-cracks in the rock sample gradually close under axial loading; the AB stage is the linear elastic phase, where the material fully recovers to its initial shape under axial loading; the BC stage is the plastic phase, where irreversible displacement of atoms within the rock sample occurs with increasing load, leading to permanent damage; point C is the peak stress, representing the maximum external load the rock sample can withstand; and the post-point C stage is the final failure phase.

Among the 12 groups of damaged rock samples, the Blank sample exhibited the highest peak stress of 260.5 MPa, while the impact-damaged sample S-Blank had a peak stress of 234.57 MPa, a 9.95% decrease. For different acid-etching durations, the peak stresses of acid-etched shales A1d, A3d, A7d, A14d, and A28d were 230.54, 213.86, 200.82, 190.08, and 180.93 MPa, with reduction rates of 11.5%, 17.9%, 22.91%, 27.03%, and 30.55%, respectively. The results indicate that acid etching significantly reduces the peak stress of rock samples, and longer acid-etching times cause more pronounced degradation of mechanical properties. Additionally, the peak stresses of combined-damage shales SA1d, SA3d, SA7d, SA14d, and SA28d with different acid-etching times were 199.49, 185.95, 163.11, 154.23, and 147.10 MPa, corresponding to reduction rates of 23.42%, 28.62%, 37.39%, 40.79%, and 43.53% compared to

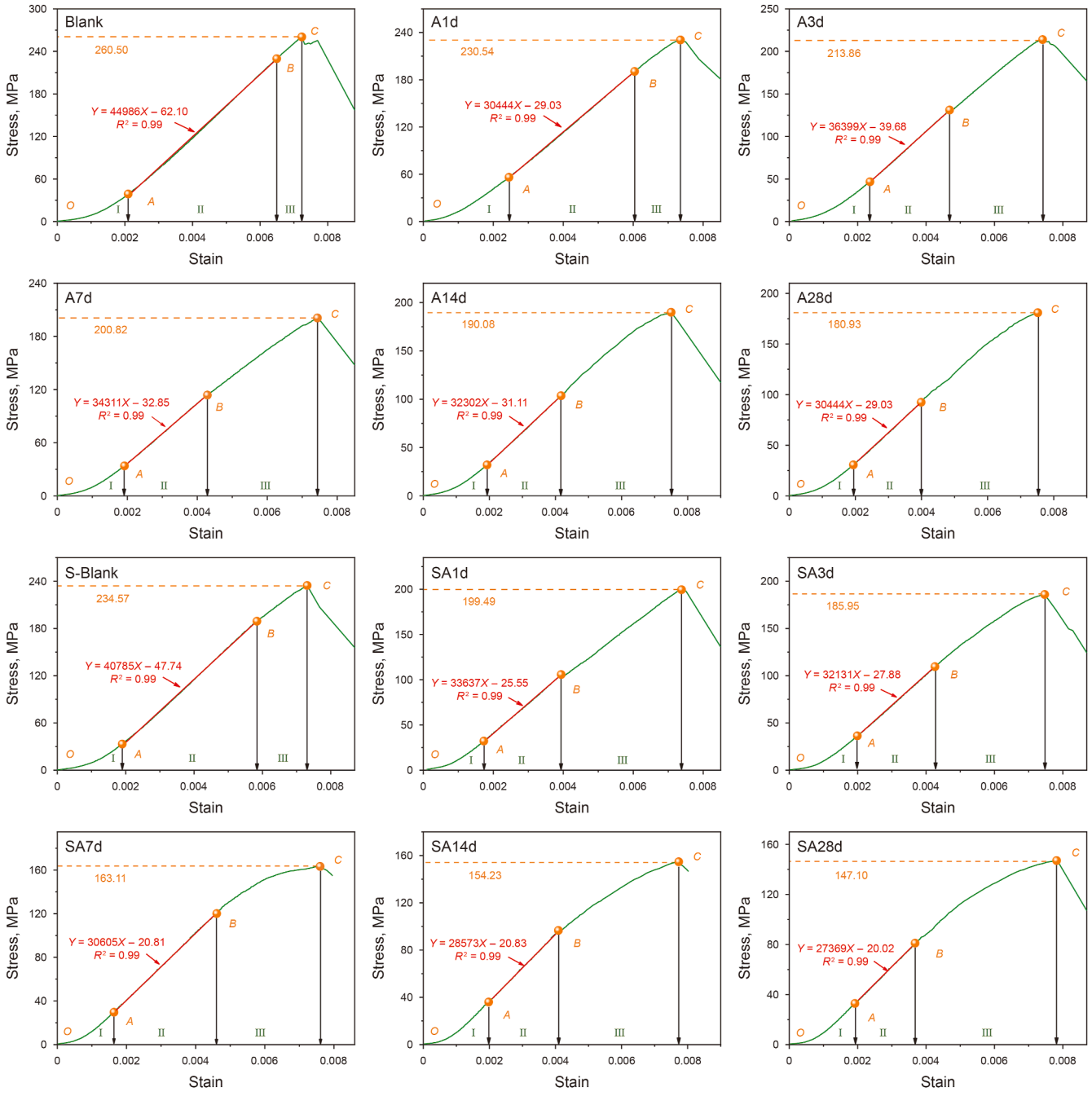

Fig. 5. Stress-strain curves of shale under 12 sets of different damage conditions.

the Blank group. Compared with acid-etched shales, combined-damage shales showed significantly higher reduction rates at the same acid-etching time, indicating that dynamic impact damage and acid etching have a synergistic degrading effect on the mechanical properties of shale. Dynamic impact damage alters the internal microstructure of shale, promoting the generation and development of micro-cracks, allowing hydrochloric acid solution to penetrate deep into the rock mass along these cracks, react with minerals over a larger area, and thus accelerate the acid-rock reaction process, further deteriorating the mechanical properties of rock samples.

The elastic modulus is an important indicator for measuring the elastic deformation capacity of materials under compressive stress (Peng et al., 2024). The elastic modulus of ordinary shale Blank was 44.99 GPa, while those of shales A1d, A3d, A7d, A14d, and A28d with different acidization times were 37.23, 36.4, 34.31, 32.3, and 30.44 GPa, with reduction rates of 17.25%, 19.09%, 23.74%, 28.21%, and 32.34% compared to the Blank group. The elastic moduli of combined-damage shales SA1d, SA3d, SA7d, SA14d, and SA28d were 33.64, 32.13, 30.61, 28.57, and 27.37 GPa, with reduction rates of 25.23%, 28.58%, 31.96%, 36.50%, and 39.16%, respectively. This indicates that acid etching and impact damage treatments degrade the internal structure of rock samples, reducing the ability of shale to maintain shape stability under compressive stress, and combined-damage treatment further increases the reduction amplitude of elastic modulus.

Furthermore, among the 12 groups of rock samples, the Blank group had the smallest peak strain (7.24×10^{-3}), while the SA28d sample had the largest peak strain (7.82×10^{-3}), which was 7.42% higher than that of the Blank sample (Table 1). The time-peak strain curves of both acid-etched and combined-damage shales showed an upward trend, indicating that damage treatments increase the peak strain of rock samples, and the peak strain is positively correlated with the acid-etching time. At the same acid-etching time, the peak strain of combined-damage shales was higher than that of acid-etched shales, suggesting that the combined damage of impact damage + acid etching has a synergistic degrading effect on rock samples.

Fig. 6 plots the variations in peak stress, peak strain, and elastic modulus of shales with different damage states based on Table 1. It can be seen that as the hydrochloric acid etching time increases, the peak stress and elastic modulus of both acid-etched and combined-damage rock samples generally show a downward trend (Fig. 6). Comparing different rock samples at the same acid-etching duration, the peak stress and elastic modulus of combined-damage samples were always lower than those of single acid-etched samples. Taking the 28-day treatment cycle as an example, the peak stress loss of the composite-damage sample

Table 1
Peak stress, peak strain and elastic modulus of shale in different damage states.

Samples	Peak stress, MPa	Peak strain, 10^{-3}	Modulus of elasticity, GPa
Blank	260.5	7.24	44.99
A1d	230.54	7.35	37.4
A3d	213.68	7.41	34.3
A7d	200.82	7.46	33.2
A14d	190.08	7.49	32.3
A28d	180.93	7.52	30.4
S-Blank	234.57	7.32	40.8
SA1d	199.49	7.38	32
SA3d	185.95	7.47	30.6
SA7d	163.11	7.67	29.2
SA14d	154.23	7.73	28.6
SA28d	147.10	7.82	27.4

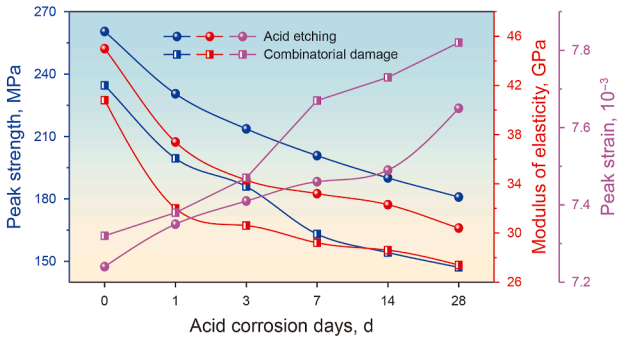

Fig. 6. Plot of peak stress, peak strain and modulus of elasticity of shale under different damage conditions.

SA28d reached 43.53%, and the elastic modulus loss was 39.16%, which were significantly higher than those of the pure acid-etched sample A28d (peak stress loss 30.55%, elastic modulus loss 32.34%). This data indicates that the synergistic effect of impact damage and acid etching has a more significant deteriorating effect on the mechanical properties of shale than single acid etching. Through the interaction of physical damage and chemical corrosion, the two significantly reduce the mechanical properties of shale materials.

3.3. Evolutionary analysis of energy dissipation in shale with different damage states

3.3.1. Principle of energy calculation

The deformation and failure processes of rocks fundamentally involve the dissipation and release of internal energy under external loads (Peng et al., 2025; Ru et al., 2024; Luo et al., 2023). When treating a volume element of rock as a closed system while under stress, we can apply the law of conservation of energy. In this case, the work done on the rock element by external forces is converted into the elastic strain energy stored in the rock sample, dissipative energy associated with irreversible deformation, and a minor amount of other forms of energy. Based on the law of conservation of energy, we derive the relationships among these energy types (Yu et al., 2023; Liu et al., 2024a, b):

$$U = U^{e} + U^{d} \tag{4}$$

In Eq. (4), U represents the total energy converted from the load, U^{e} denotes the stored elastic strain energy, and U^{d} represents the dissipative energy during the energy conversion process. The relationships among the three types of energy in the sealed material under axial load are illustrated in Fig. 7:

Thus, the elastic strain energy per unit volume of the sealing material is expressed as:

$$U^{e} = \frac{1}{2}\sigma_1\varepsilon_1^{e} + \frac{1}{2}\sigma_2\varepsilon_2^{e} + \frac{1}{2}\sigma_3\varepsilon_3^{e} \tag{5}$$

where σ_1, σ_2 and σ_3 are the stresses of the presses that the material is subjected to in the three directions, respectively; ε_1^{e}, ε_2^{e} and ε_3^{e} are the strains corresponding to the stresses, respectively.

According to Hooke's law, Eq. (5) can be transformed into:

$$U^{e} = \frac{\sigma_1^2}{2E} \tag{7}$$

Additionally, applying the concept of definite integrals, the total energy U is calculated as:

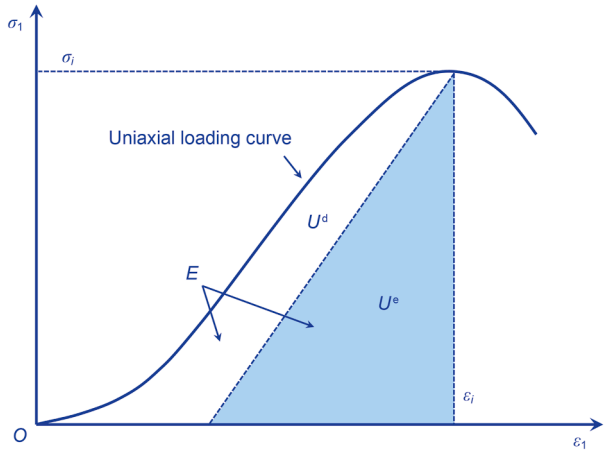

Fig. 7. Three energy relations for rock samples under uniaxial loading.

$$U = \int \sigma_1 \mathrm{d}\varepsilon_1 = \sum_{i=1}^{n-1} \int_{\varepsilon_i}^{\varepsilon_{i+1}} \sigma_i \mathrm{d}\varepsilon_1 = \sum_{i=1}^{n=1} \frac{\varepsilon_{i+1} - \varepsilon_i}{2} (\sigma_{i+1} + \sigma_i) \tag{8}$$

where σ_i and ε_i refer to the stress and strain values of the sealing material at specific points along the stress-strain curve, respectively. Therefore, the dissipated energy U^d of the sealing material during deformation and failure can be expressed as:

$$U^d = U - U^e \tag{9}$$

3.3.2. Laws of energy evolution

Analyzing energy variations reveals the deformation and failure mechanisms of rocks under different loading conditions. The total energy U, elastic strain energy U^e, and dissipated energy U^d of 12 shale groups during deformation and failure were calculated using Eqs. (7)–(9). As shale is a brittle material without post-peak behavior, the pre-peak stage of the stress-strain curve was selected for energy calculation, yielding the relationship between energy parameters and stress-strain curves for each group (Fig. 8) (Yu et al., 2023; Ozoji et al., 2024).

The evolution curves of strain and the three energy components are divided into three stages: micro-crack closure (Stage I), elastic deformation (Stage II), and plastic deformation (Stage III). In Stage I, internal pores of the rock sample gradually close under the testing machine's load. Part of the applied energy converts to elastic strain energy, while the rest becomes irreversible dissipated energy, with all three energy curves growing slowly. Stage II is the linear elastic phase, where the applied load primarily converts to elastic strain energy. Elastic strain energy and total energy increase steadily with similar trajectories, while dissipated energy remains unchanged. Stage III is the plastic phase, where microcrystalline friction and dislocation movement convert more energy to dissipated energy, slowing the growth rate of elastic strain energy and accelerating that of dissipated energy.

In the energy evolution curves of 12 shale groups, the elastic strain energy and total energy curves of the Blank sample show highly similar growth rates and trajectories for most periods, while dissipated energy grows slowly or stagnates, only increasing slightly at the curve's end. This indicates the Blank sample has minimal micro-crack development, a dense and uniform microstructure, and strong deformation resistance. However, damaged samples exhibit diversified changes in Stage III: total energy grows steadily, elastic strain energy slows, the gap between them widens, dissipated energy increases significantly, and its growth trend correlates with the damage degree. This is because damage treatment increases internal micro-cracks and reduces rock homogeneity. External loading induces uneven stress in damaged samples, promoting crack growth and network formation, causing local structural damage, releasing elastic strain energy, decreasing its growth rate, and rapidly increasing dissipated energy.

3.3.3. Energy evolution of shale with different damage states

To analyze energy evolution, relationships between the three energy parameters and strain for 12 material groups were plotted (Figs. 9–11). The total energy curve is divided into slow growth (0–0.001), stable growth (0.001–0.005), and rapid growth (> 0.005) stages (Fig. 9). The total energies of Blank, A1d, A3d, A7d, A14d, A28d, S-Blank, SA1d, SA3d, SA7d, SA14d, and SA28d are 0.789, 0.772, 0.720, 0.693, 0.685, 0.669, 0.744, 0.688, 0.711, 0.656, 0.636, and 0.625 kJ/m^3, respectively. Total energy comprehensively reflects material strength, toughness, and durability, indicating the ability to absorb and disperse external loads. The Blank sample has the highest total energy, while damaged samples show reduced total energy, demonstrating that damage treatment weakens shale's load absorption and dispersion capacity. Additionally, combined-damage samples have lower total energy than acid-etched samples at the same acid-etching time, confirming that combined damage deteriorates total energy more significantly, with longer acid-etching times enhancing this effect.

The elastic strain energy-strain curves of 12 shale groups are divided into slow growth (0–0.001), steady growth (0.001–0.005), and disordered growth (> 0.005) stages (Fig. 10). The first two stages show similar trends to total energy, indicating that minor deformations store most axial load energy in a stable state. The third stage exhibits significant differences: the Blank sample maintains high elastic strain energy growth, while damaged shales (A1d, A3d, A7d, A14d, A28d, SA1d, SA3d, SA7d, SA14d, SA28d) show reduced elastic strain energy (0.714, 0.628, 0.573, 0.559, 0.53, 0.592, 0.580, 0.436, 0.419, 0.395 kJ/m^3, respectively).

The dissipated energy-strain curves (Fig. 11) are divided into slow growth (0–0.001), stagnant growth (0.001–0.005), and rapid growth (> 0.005) stages. During stagnant growth, dissipated energy initially grows uniformly but stagnates in the middle-late stage. In the rapid growth stage, damaged shales show higher growth rates than the Blank group, indicating that damage treatment increases micro-cracks and local damage, consuming more energy to overcome inter-granular slip and deformation. Combined-damage shales have higher dissipated energy growth rates than acid-etched shales at the same acid-immersion time, confirming that dynamic impact and acid etching synergistically promote crack extension, increasing energy dissipation. Longer acid-immersion times enhance peak failure dissipated energy, aggravating shale deterioration and micro-deformation energy dissipation.

Fig. 12 shows the relationship between energy parameter peaks and acid treatment time: total energy and elastic strain energy decrease, while dissipated energy increases with prolonged acid treatment. Combined damage exacerbates internal deterioration, leading to lower total/elastic strain energy and higher dissipated energy than single acid etching, verifying that combined damage introduces more structural defects, reducing energy storage capacity.

Analyzing the ratio of dissipated energy to total energy at failure (Fig. 13) reveals: Blank, A1d, A3d, A7d, A14d, A28d, S-Blank, SA1d, SA3d, SA7d, SA14d, SA28d have dissipated energy ratios of 4.51%, 7.51%, 12.70%, 17.31%, 18.4%, 20.86%, 9.44%, 14.02%, 18.53%, 33.57%, 34.16%, and 34.74%, respectively. Combined-damage samples exhibit higher ratios than acid-etched ones at the same acid-etching time (e.g., SA28d's 34.74% vs. A28d's 20.86%), confirming the synergistic effect of impact damage and acid etching. Longer

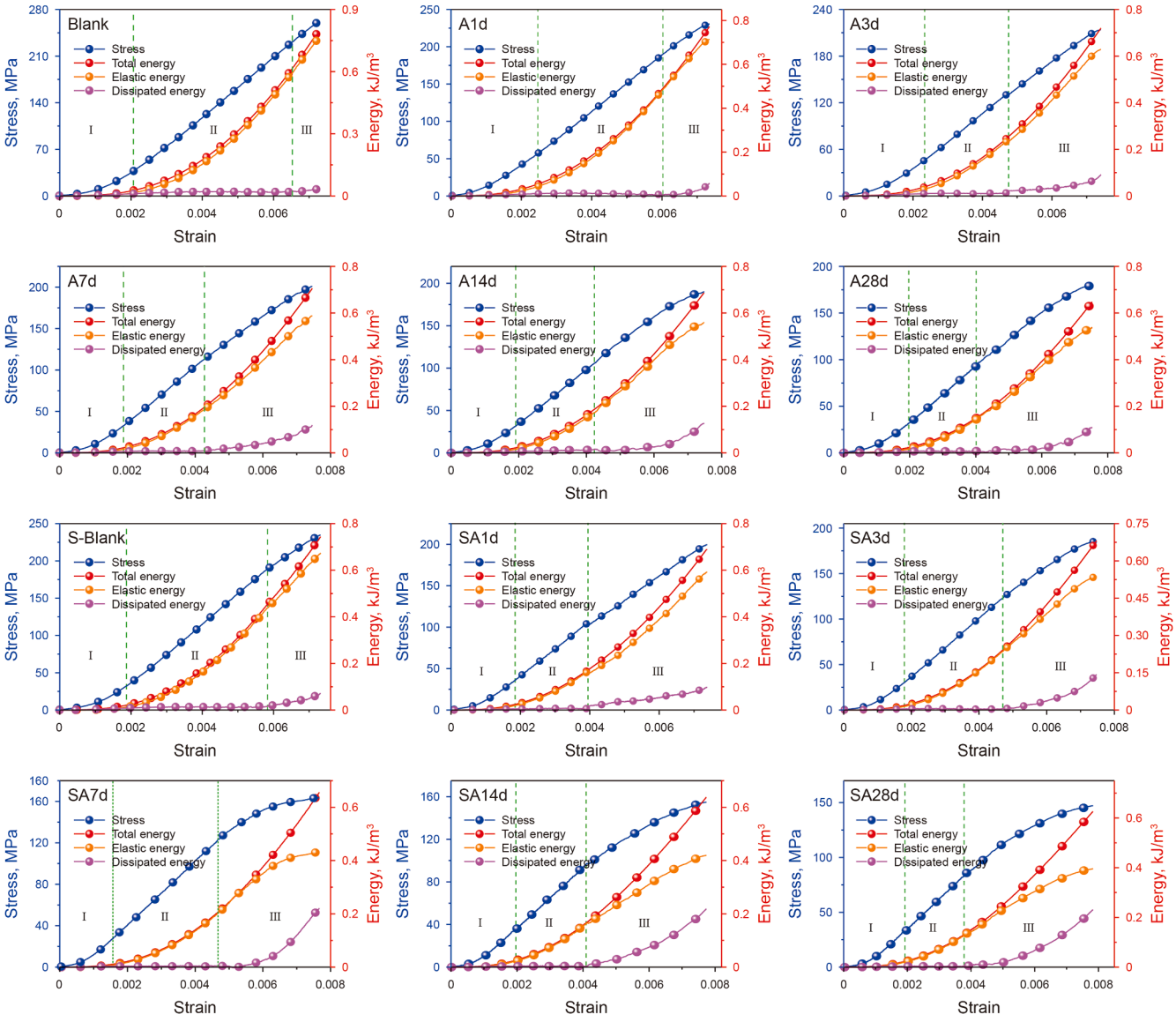

Fig. 8. Energy evolution relationship curves for shales of 12 groups.

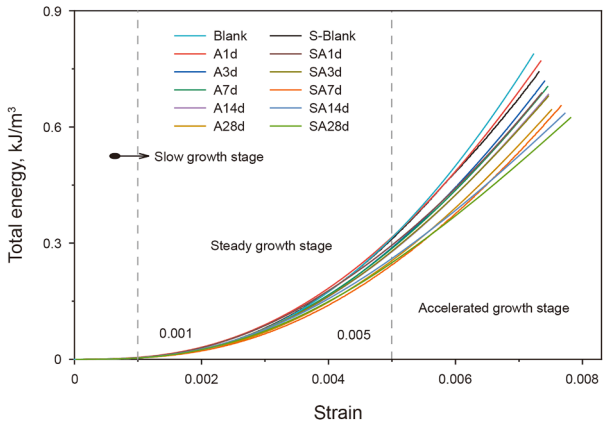

Fig. 9. Plot of total energy versus strain for 12 shale groups.

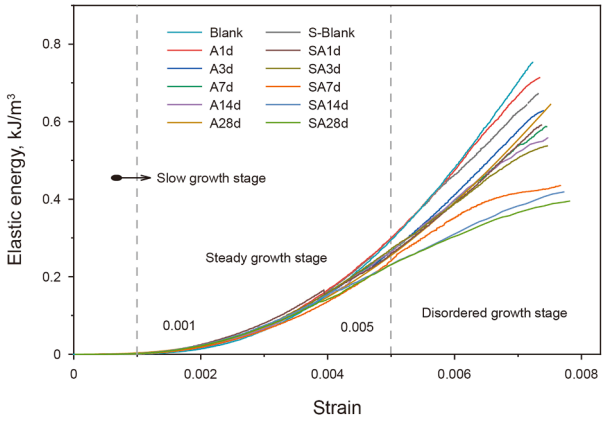

Fig. 10. Plot of elastic energy versus strain for 12 shale groups.

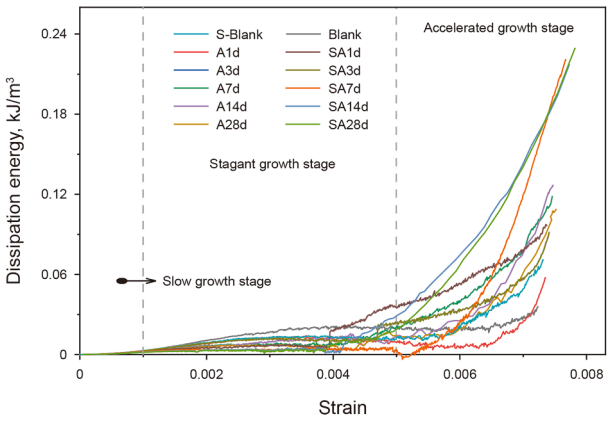

Fig. 11. Plot of dissipation energy versus strain for 12 shale groups.

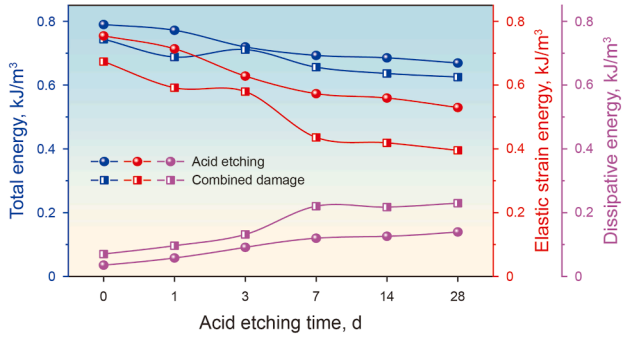

Fig. 12. Relationship between the peak energy values of 12 groups of shales and acid treatment time.

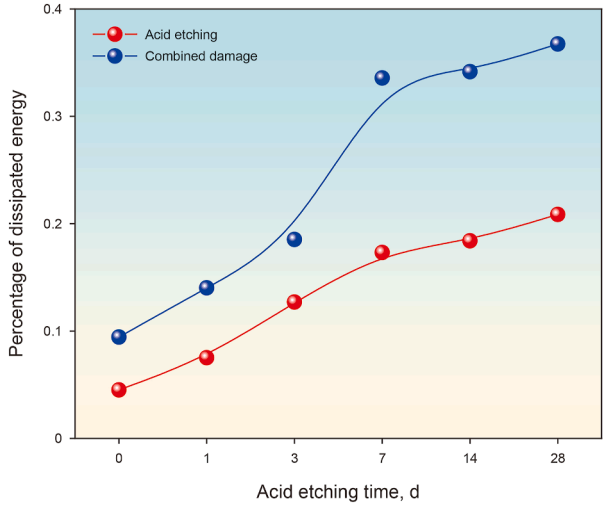

Fig. 13. Dissipated energy share at destruction for 12 shale groups.

acid-etching times increase the ratio due to deeper acid penetration, broader pore formation, reduced homogeneity, and more energy consumed for inter-granular slip under external loading.

3.4. XRD experimental study on shale with different damage states

XRD tests were conducted on 12 groups of shale samples to analyze the effects of different treatments on mineral composition and structure. The XRD patterns of all samples showed multiple high-intensity diffraction peaks (Fig. 14). Calcite and ankerite, two carbonate minerals, were analyzed. Results showed that although XRD patterns of all samples were highly similar, containing calcite and ankerite, the intensities of diffraction peaks varied significantly. Specifically, the diffraction peak intensities of Blank and S-Blank samples were notably higher than those of acid-immersed samples, indicating that acid immersion effectively reduces the carbonate content in shale, reflecting the dissolution of acid on carbonate minerals. For samples immersed for 3 days, the diffraction peak intensity was lower than that of 1-day treated samples, and further decreases were observed in 7-day and 14-day treated samples. The diffraction peaks of 28-day treated samples were significantly lower than other groups, suggesting that prolonged acid immersion helps further reduce carbonate content. Additionally, comparing composite-treated samples with pure acid-immersed ones, the diffraction peaks of calcite and ankerite in composite-treated samples were significantly reduced, further indicating that composite treatment accelerates the reaction between rock and acid, thereby enhancing the acid-rock reaction rate.

3.5. Analysis of shale microstructure and image binarization processing

As inferred from the previous section, the reaction between hydrochloric acid and shale effectively reduces its carbonate content. Therefore, SEM was used to microscopically observe shale, investigating the effects of damage treatments on surface particle morphology, size, and pore status (Chen et al., 2019; Huang et al., 2024a, b; Jing et al., 2023). Fig. 15 displays the microscopic images of 12 shale groups under 1000× magnification. The microstructure of ordinary shale (Blank and S-Blank) is the densest, with white mineral particles tightly embedded, minor micro-pores and cracks at the interface, poor pore development and connectivity, exhibiting high bearing capacity and recovery performance. In contrast, the microstructures of acid-etched samples (A1d, A3d, A7d, A14d, A28d) and combined-damage samples (SA1d, SA3d, SA7d, SA14d, SA28d) have undergone significant changes. White particles are drastically reduced, and dense, unevenly distributed pores appear at the interface. With the increase in acid immersion time, the number and size of pores significantly expand. The occurrence and expansion of these pores introduce numerous defects into the shale, weakening the bearing skeleton and significantly reducing bearing capacity and recovery ability, verifying the test results in

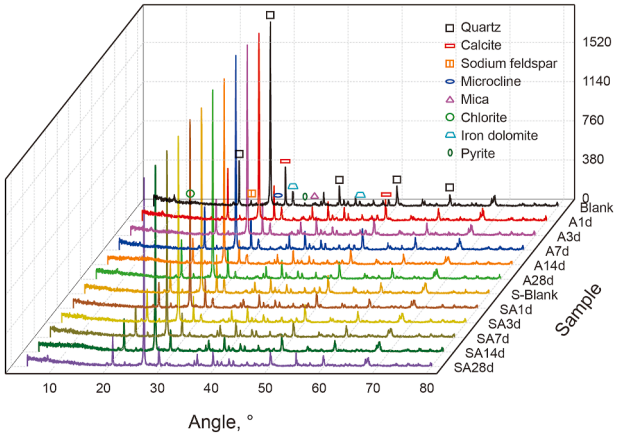

Fig. 14. XRD results of 12 sets of rock samples.

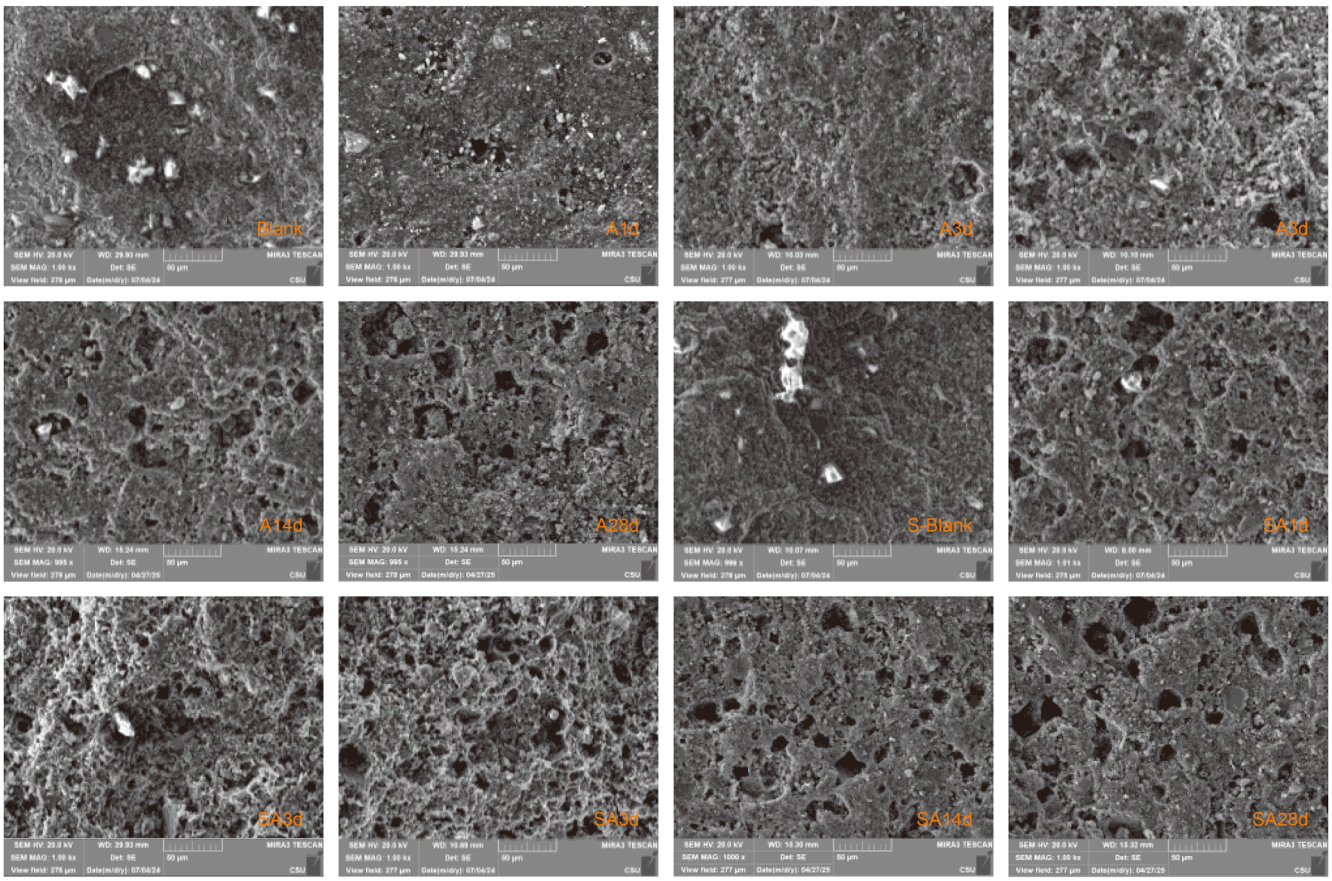

Fig. 15. SEM images of 12 groups of shale.

Section 3.2. Additionally, comparing acid-etched samples with combined-damage samples, even at the same acid immersion concentration, combined-damage samples show larger pore sizes and more developed pore structures, indicating that combined damage effectively promotes the contact between acid solution and ore body, enhances the degree of acid-rock reaction, and further triggers the internal structural degradation of shale.

Binary processing of images simplifies them into black and white, enhancing feature extraction and noise suppression, and improving the efficiency and accuracy of analysis. In the figures, white represents the shale matrix, and black indicates pores (Huang et al., 2024a, b). The SEM images in Fig. 15 have been converted into binary images (Fig. 16). In Blank and S-Blank samples, there are a few small black dots and slender strips, while acid-etched and combined-damage shales exhibit more large black areas. These black areas are more densely distributed and have enhanced connectivity, suggesting that acid etching promotes pore generation and area proportion. As acid etching time increases, the density and connectivity of black areas enhance, indicating that prolonged hydrochloric acid immersion effectively improves mineral solubility, forms a more complex pore network, and enhances the fragmentability of rock samples. Compared with single acid-etched samples, combined-damage samples have a larger number of large-sized black areas with denser distribution.

To deeply investigate the pore structure distribution characteristics of shale, ImageJ image processing technology was used to process the binarized images in Fig. 16, obtaining the pore parameters of 12 groups of rock samples (Table 2). Furthermore, the total area comparison diagram of different pore sizes in shale (Fig. 17) and the stacked diagram of pore size area proportion (Fig. 18) were drawn. The pores of rock samples are divided into small pores (0–5 μm^2), medium pores (5–10 μm^2), and large pores (> 10 μm^2). The untreated shale has the largest total area of small pores, followed by the area of medium pores, while the total area of large pores is extremely small (Fig. 18). Damage treatments have little effect on small pores but significantly increase the total area of medium and large pores. With the increase of acid etching time, the total area of medium and large pores in acid-etched and combined-damage treated rock samples gradually increases, and the damage treatment has the most significant effect on the total area of large pores. In addition, under the same acid etching time, the total area of medium and large pores in combined-damage shale is higher than that in acid-etched-only shale.

Furthermore, the total porosities of the 12 shale groups are 2.28%, 4.58%, 5.55%, 8.35%, 10.41%, 14.6%, 2.58%, 9.45%, 12.35%, 15.86%, 17.59%, and 23.87%, respectively. The pore proportion of acid-etched shales is significantly higher than that of Blank and S-Blank shales. The porosities of acid-etched shales are in the order of A1d, A3d, A7d, SA1d, A14d, SA3d, A28d, SA7d, SA14d, and SA28d. The combined-damage sample SA7d has the highest porosity, which is 15.06% higher than that of the Blank sample. Acid etching and combined-damage treatments have the most significant impact on the macropores of shale. The macropore proportion of the untreated sample is 0.18%, and those of the treated samples are 2.83%, 3.5%, 5.52%, 8.21%, 11.91%, 7.49%, 8.97%, 12.26%, 14.56%, and 20.18%, respectively (Fig. 18). With the increase in acid etching time, the macropore proportion shows an increasing trend. Among them, SA28d has the highest macropore proportion, which is 20% higher than that of the Blank sample. Moreover, the porosity and macropore proportion of combined-damage shales are higher than

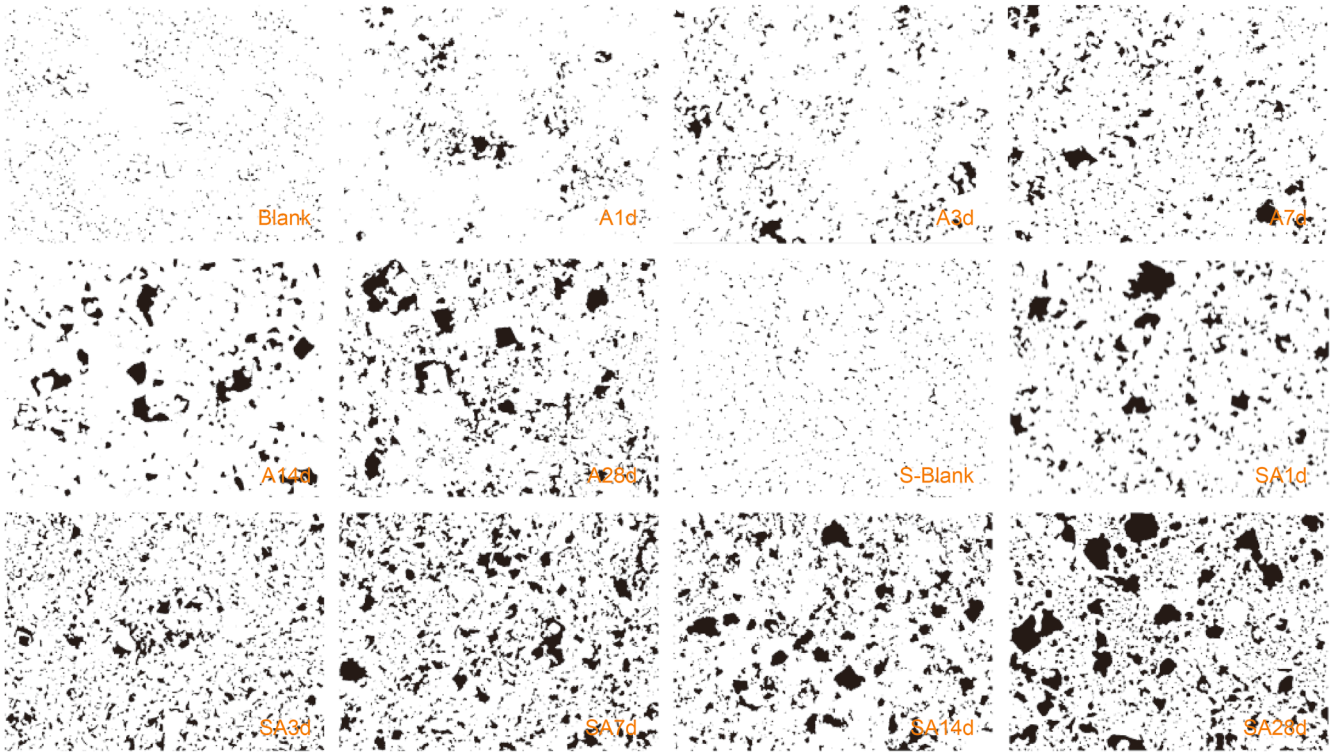

Fig. 16. Binarized image processing results.

those of single acid-etched shales, indicating that combined damage improves the damage and degradation effect of rock samples, contributing to enhancing the pore connectivity and gas permeability of shale.

3.6. Evolution analysis of pore structure in shale with different damage states

At constant temperature, the adsorption properties of porous materials correlate with pressure, resulting in different types of adsorption isotherms that describe the adsorption of gases or liquids on solid surfaces (Wang et al., 2022; Li et al., 2022). The low-temperature nitrogen adsorption isotherms of shale show that the nitrogen adsorption capacity gradually stabilizes with increasing relative pressure (Fig. 19), rising significantly when the relative pressure exceeds 0.8. According to IUPAC classification, the adsorption isotherms of the samp les conform to Type IV, and the desorption hysteresis loops conform to Type H3 hysteresis.

Based on the BET (Zhang et al., 2022) and Kelvin equations (Wen et al., 2023), when the relative pressure $P/P_0 < 0.2$, monomolecular layer adsorption of nitrogen occurs on the shale surface; when P/P_0 is between 0.2 and 0.8, multi-layer adsorption dominates; when P/P_0 exceeds 0.8, the isothermal adsorption curve rises rapidly, indicating capillary condensation of nitrogen in the rock sample. In Type IV isotherms, obvious desorption hysteresis occurs, and the type of hysteresis loop is related to the pore structure of shale. The hysteresis loops of untreated Blank and S-Blank samples are wide, indicating that nitrogen enters narrow throat pores during adsorption and requires higher pressure during desorption, suggesting poor pore connectivity in untreated shale (Fig. 19). After acid-etching and impact damage treatments, the hysteresis loops of rock samples narrow, indicating that hydrochloric acid solution etching can open semi-closed or closed pores, transforming the pore structure from cylindrical to more open cylindrical, thus optimizing pore connectivity. Comparing the effects of different acid-etching times and treatment methods on the isothermal adsorption curves, prolonged acid immersion and composite treatment significantly narrow the hysteresis loops and increase nitrogen adsorption during the adsorption stage, indicating that acid-etching degrades the microstructure of shale.

The NLDFT method based on non-local density functional theory was used to analyze the isothermal adsorption curves, enabling the acquisition of pore distribution within the range of 0–250 nm in rock samples and the analysis of micropores (< 2 nm), mesopores (2–50 nm), and macropores (> 50 nm) to describe rock sample characteristics (Li et al., 2020; Li et al., 2025a, b; Ma et al., 2024) (Table 3). The red curve in Fig. 20 represents the incremental pore volume of the rock sample, while the blue curve reflects changes in cumulative pore volume. The incremental pore volume curve shows that the micropore volume of shale is relatively small, while the volumes of mesopores and macropores are significantly larger. Analysis of the cumulative curve and Table 3 reveals that the cumulative pore volume of untreated shale is the lowest, indicating poor pore connectivity. After acid-etching treatment, the cumulative pore volume increases significantly, suggesting that acid-etching effectively enhances the total porosity of rock samples. As the acid-etching time prolongs, the pore volume of rock samples gradually increases, indicating that prolonged acid immersion further degrades the internal structure of rock samples. It is noteworthy that the pore volume of composite-treated shale is significantly larger than that of acid-etched shale alone.

To investigate the effects of different damage treatments on the pore volume of shale, the pore volume data for micropores (< 2 nm), mesopores (2–50 nm), and macropores (> 50 nm) were compiled (Table 3) and plotted as percentage stacked bar charts (Fig. 21). Fig. 21 shows that the distribution of the three pore

Table 2
Pore parameters of 12 groups of rock samples.

No.	Aperture range, μm²	Quantity	Total area, μm²	Average aperture, μm²	Percentage of area, %
Blank	> 0	877	1309.54	1.49	2.28
	0–5	842	1023.38	1.22	1.78
	5–10	28	182.32	6.51	0.32
	> 10	7	103.84	14.83	0.18
A1d	> 0	651	2402.96	4.00	4.58
	0–5	555	655.87	1.18	1.15
	5–10	48	335.29	6.99	0.59
	> 10	48	1411.80	33.58	2.84
A3d	> 0	1001	3610.32	2.91	5.55
	0–5	875	1135.13	1.30	1.24
	5–10	79	544.42	6.89	0.81
	> 10	53	1930.77	23.22	3.50
A7d	> 0	836	4744.62	5.68	8.35
	0–5	658	983.64	1.49	1.73
	5–10	88	622.54	7.07	1.10
	> 10	90	3138.44	34.87	5.52
A14d	> 0	1171	6026.70	5.15	10.41
	0–5	986	861.37	0.87	1.10
	5–10	97	787.71	8.12	1.11
	> 10	113	4377.62	38.74	8.21
A28d	> 0	991	8573.19	8.65	14.60
	0–5	734	918.44	1.25	1.56
	5–10	110	960.44	8.73	1.13
	> 10	147	6694.31	45.54	11.91
S-Blank	> 0	784	1512.15	1.93	2.60
	0–5	725	1074.92	1.48	1.85
	5–10	52	336.03	6.46	0.58
	> 10	7	101.20	14.46	0.17
SA1d	> 0	756	7704.96	10.19	9.45
	0–5	521	1042.73	2.00	1.13
	5–10	93	766.93	8.23	0.83
	> 10	142	5895.31	41.53	7.49
SA3d	> 0	1348	9012.71	6.69	12.35
	0–5	839	1567.23	1.87	1.76
	5–10	123	1086.96	8.84	1.61
	> 10	355	6358.53	17.91	8.97
SA7d	> 0	1193	10716.12	8.98	15.86
	0–5	826	1259.61	1.52	1.76
	5–10	128	968.32	7.57	1.83
	> 10	599	8488.19	14.17	12.26
SA14d	> 0	1412	11212.52	7.94	17.59
	0–5	576	425.37	0.74	1.05
	5–10	167	1506.22	9.02	1.98
	> 10	669	9280.93	13.87	14.56
SA28d	> 0	1546	13732.93	8.88	23.87
	0–5	581	311.51	0.54	1.58
	5–10	181	1682.35	9.29	2.11
	> 10	784	11739.07	14.97	20.18

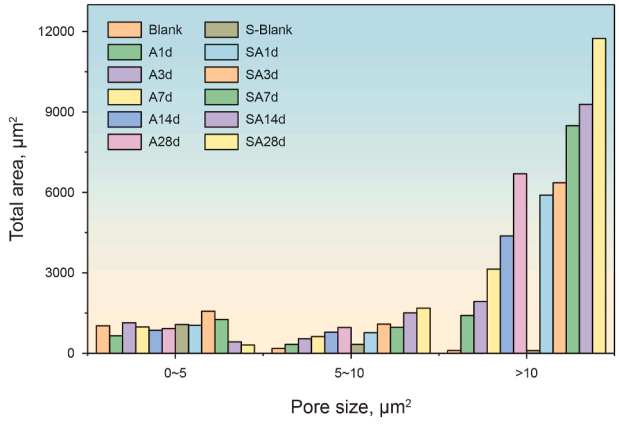

Fig. 17. Comparison of total area of different pore sizes for 12 groups of rock samples.

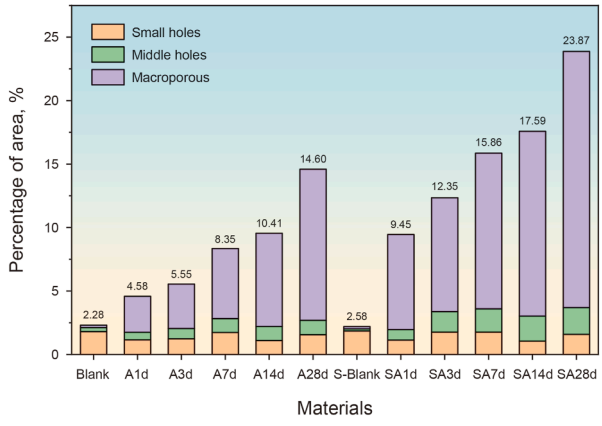

Fig. 18. Porosity stacks for different pore sizes for 12 sets of rock samples.

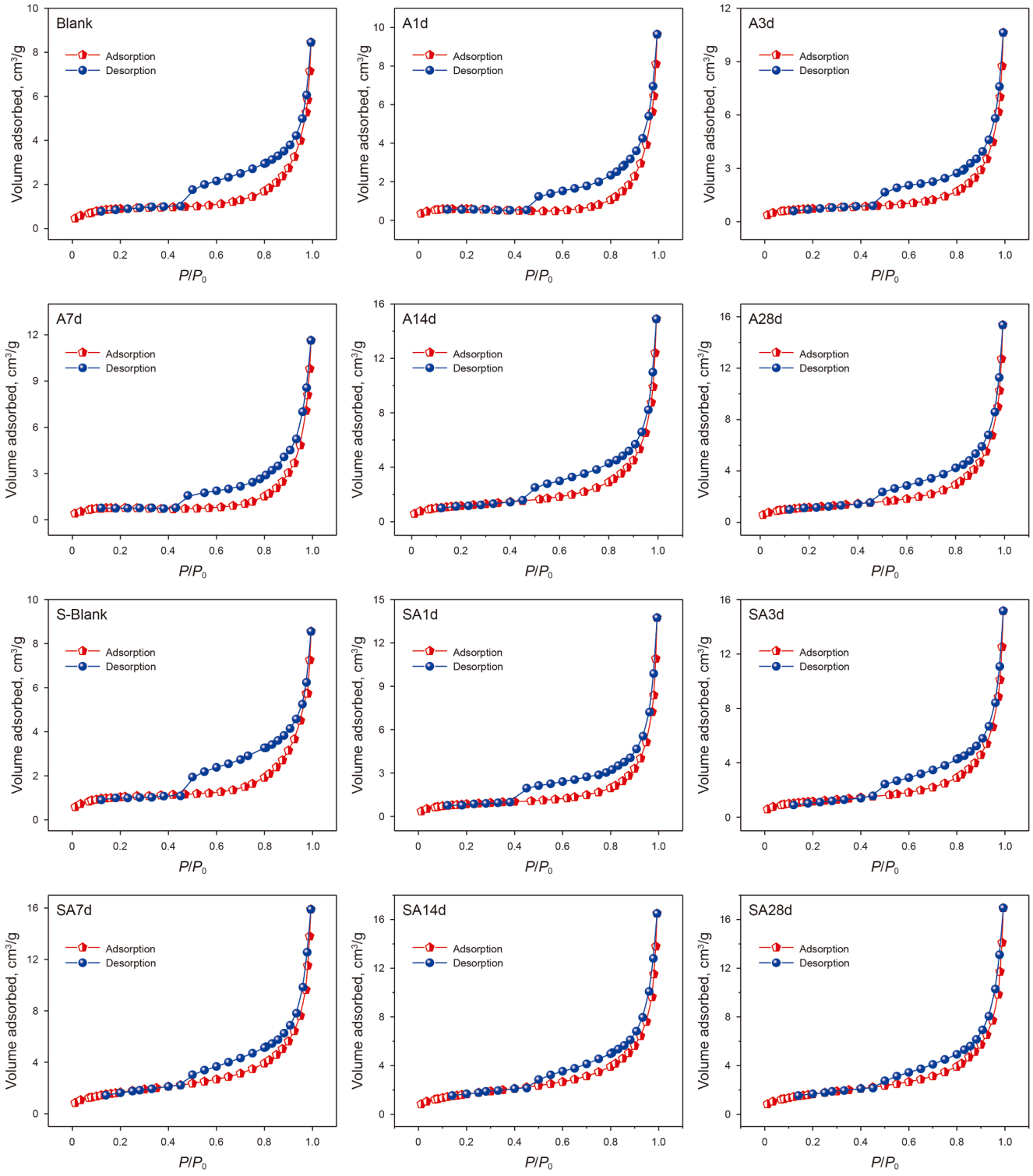

Fig. 19. Nitrogen adsorption isotherms of shale after different treatments.

volume ratios in rock samples exhibits an obvious stepwise characteristic. Acid-etching treatment reduces the volume ratio of micropores while increasing the proportions of mesopores and macropores. With the extension of acid immersion time, the proportions of mesopores and macropores in shale gradually increase, indicating that acid immersion optimizes the pore structure of rock samples. Furthermore, the composite treatment of impact damage and acid immersion significantly increases the proportions of mesopores and macropores in rock samples compared to acid-etching alone, with SA28d shale having the highest proportions of mesopores and macropores, indicating a significant synergistic effect between impact damage and acid-etching treatments in enhancing pore expansion, which is consistent with the analysis results in Section 3.4.

Table 3
Pore volume of materials.

Sample	Pores volume, $cm^3/g{\cdot}nm$			
	V_{Mic}	V_{Mes}	V_{Mac}	V_{Total}
Blank	0.00192	0.00636	0.00399	0.01226
A1d	0.00213	0.00831	0.00551	0.01595
A3d	0.00166	0.00908	0.00589	0.01663
A7d	0.00155	0.01124	0.00732	0.02012
A14d	0.00102	0.01174	0.00827	0.02103
A28d	0.00075	0.01241	0.00868	0.02184
S-Blank	0.00201	0.00661	0.00427	0.01289
SA1d	0.00101	0.01155	0.00755	0.02011
SA3d	0.00077	0.01262	0.00827	0.02166
SA7d	0.00035	0.01439	0.00952	0.02427
SA14d	0.00018	0.01507	0.01011	0.02536
SA28d	0.00007	0.01556	0.01044	0.02607

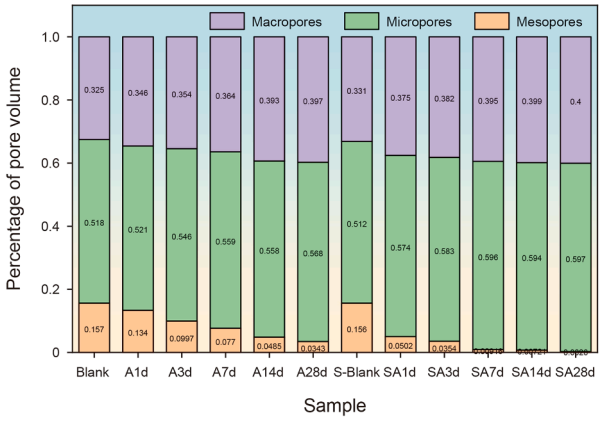

Fig. 21. Proportions of pore volume in rock samples.

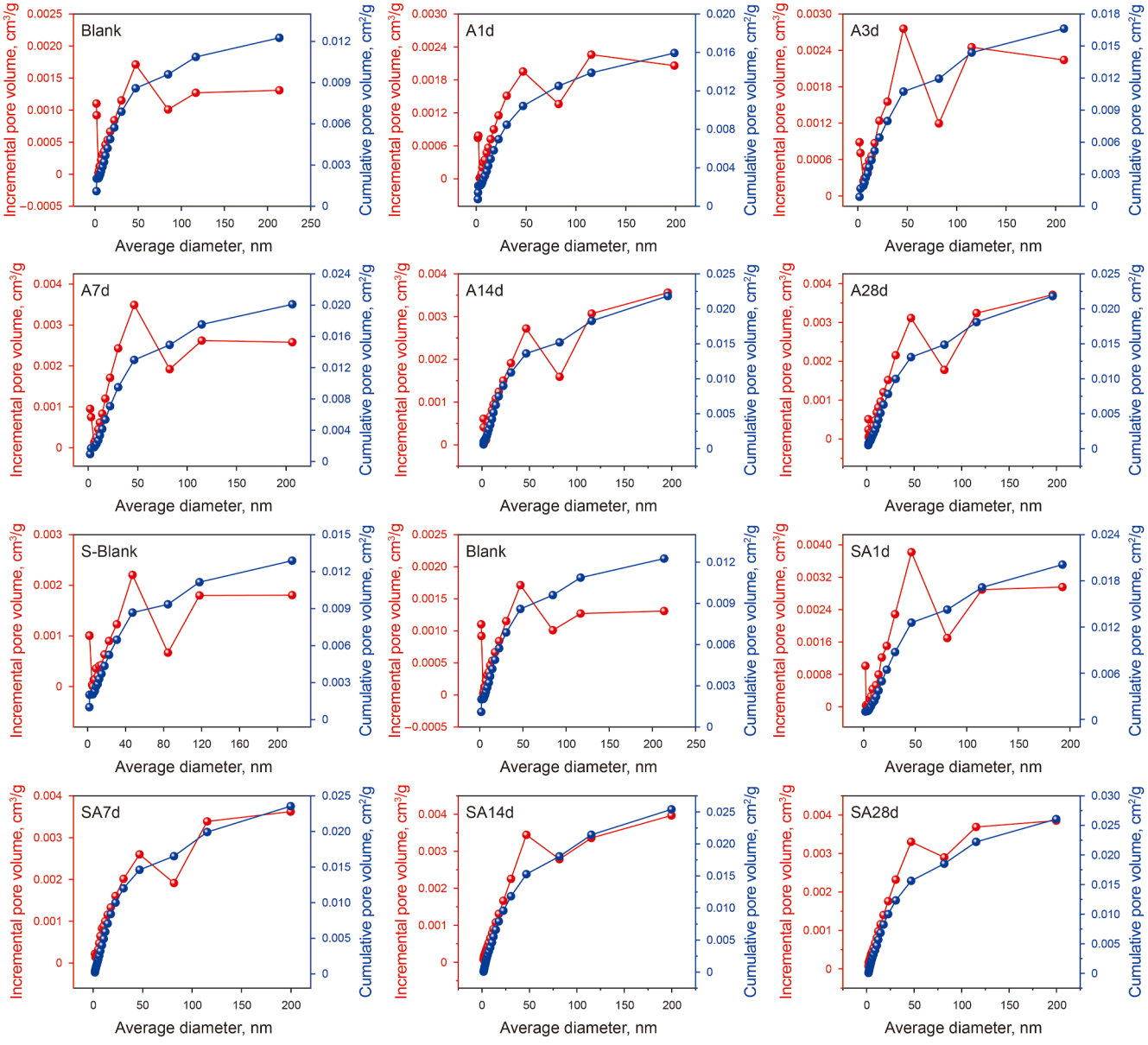

Fig. 20. Nitrogen adsorption isotherms of shale after different treatments.

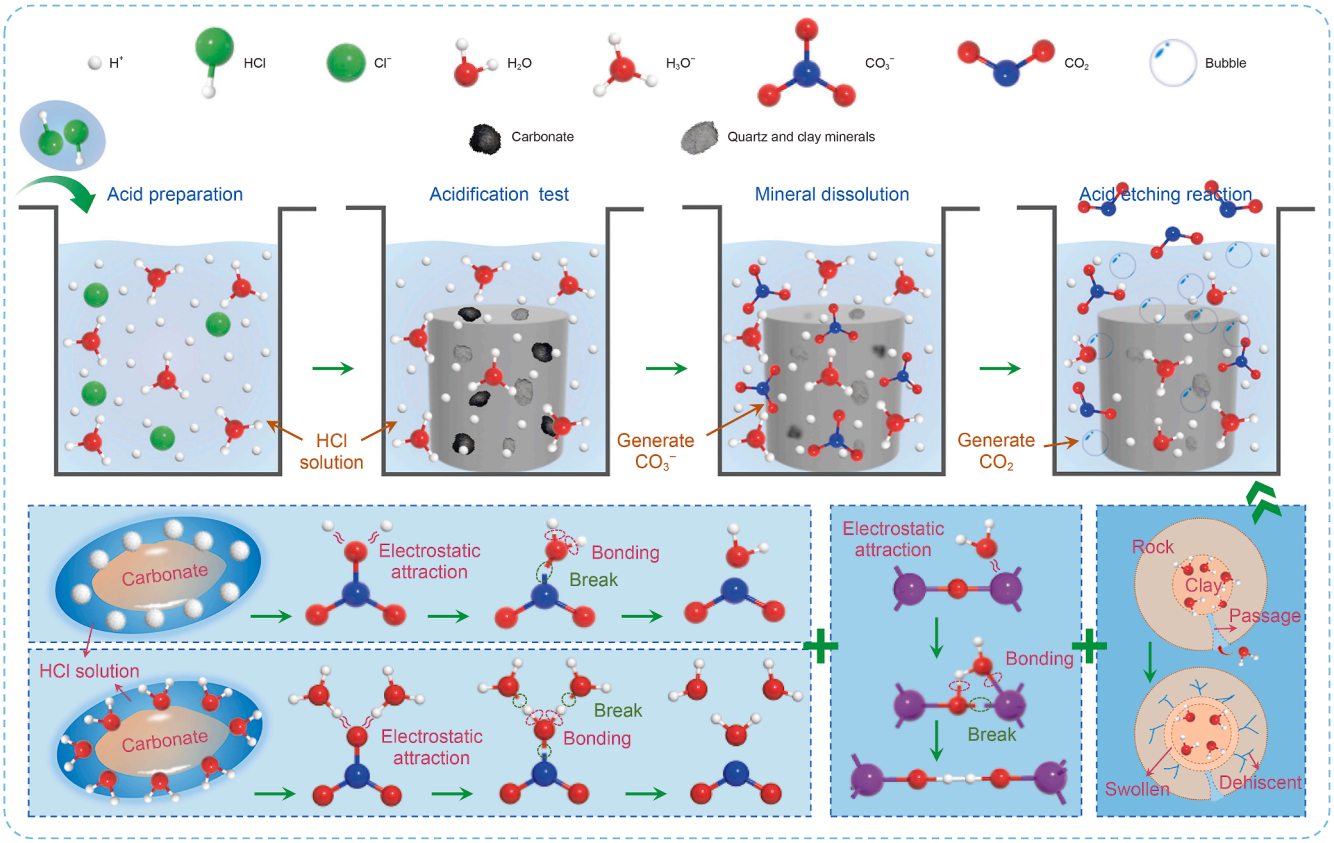

Fig. 22. Mechanism of weakening in shale.

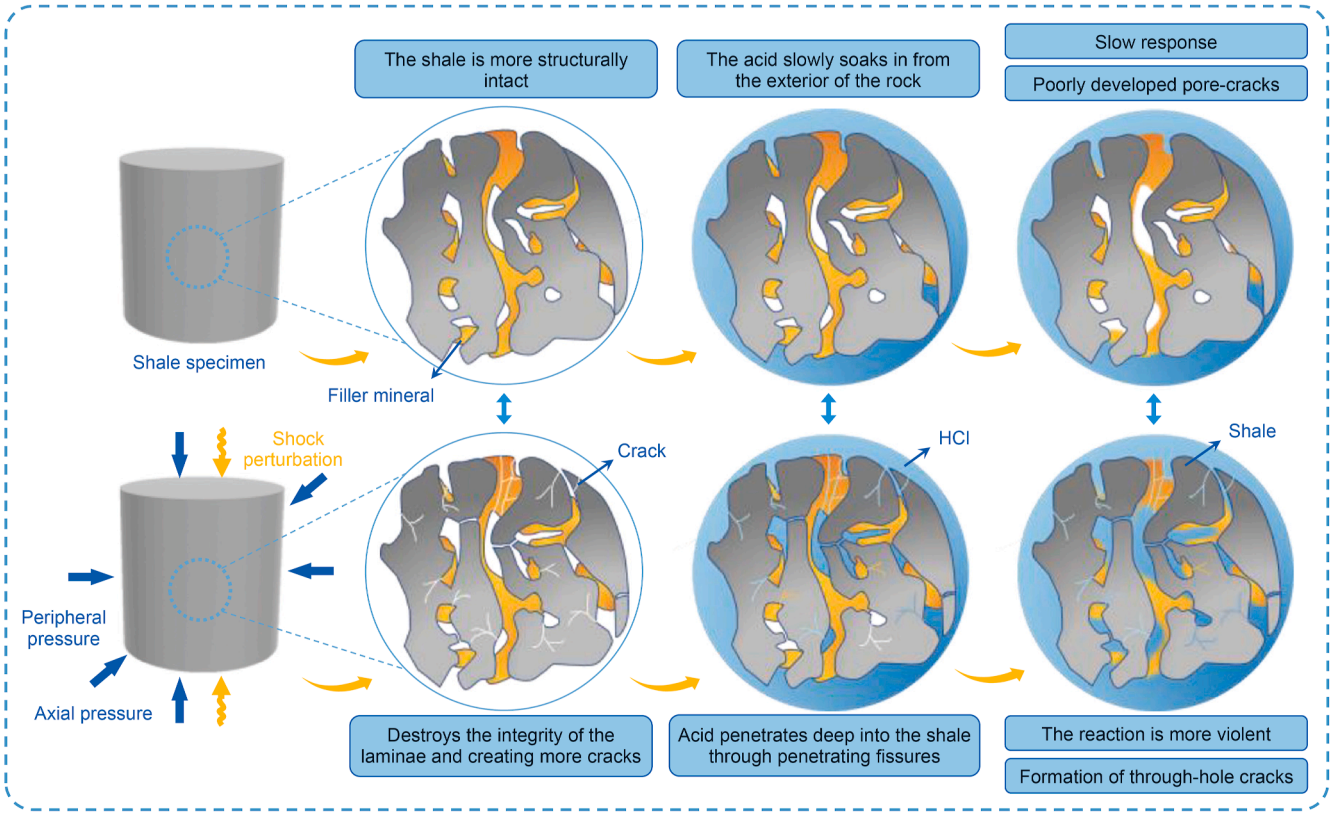

Fig. 23. Schematic of damage degradation in acid-eroded and combined damaged shales.

3.7. Damage degradation mechanism of shale

Shale is primarily composed of clay minerals, quartz, and organic matter, formed through sedimentation, compaction, and diagenesis, which transform into oil and natural gas under suitable conditions (Tian et al., 2024). During shale gas extraction using perforation-acidizing technology, acid solutions react with carbonate and clay minerals in shale. Hydrochloric acid dissociates into hydrogen ions (H^+) and chloride ions (Cl^-) in water, with part of H^+ reacting with water to form hydronium ions (H_3O^+). When shale contacts acidic solutions, carbonate minerals dissolve, releasing carbonate ions (CO_3^{2-}) and corresponding metal ions. H_3O^+ and H^+ react with CO_3^{2-} via charge attraction to generate carbon dioxide and water. Meanwhile, clay minerals undergo hydrolysis: water molecules break Si–O–Si bonds, forming weakly bonded Si–OH bonds, which expand clay layer spacing, cause clay mineral swelling, reduce mineral structural strength, and optimize shale fracturing and permeability (Fig. 22).

In acid-etching experiments, acid solutions contact carbonate and clay minerals on the rock surface, triggering acidification reactions that dissolve minerals to form pores. Ordinary shale has fewer micro-pores and poor connectivity between primary pores, with tight vertical bedding, leading to low acid-etching reaction rates and inadequate pore-fracture development. However, dynamic impact damage generates micro-cracks within shale, providing channels for acid solutions to penetrate deep into the rock and react with underlying minerals, accelerating mineral dissolution. At the same acid-etching time, the sample forms more dissolution pores and connected fractures, enhancing heterogeneity and looseness, thus reducing mechanical properties and intensifying shale damage degradation (Fig. 14). This contributes to improving downhole shale fracturing permeability and enhancing shale gas extraction efficiency (Fig. 23).

4. Conclusions

This study employed the SHPB technique to prepare dynamically impacted rock samples under three-dimensional stress, simulating actual perforation fracturing operations. The damaged shale samples, along with undamaged samples, were subsequently soaked in a 15% hydrochloric acid solution to prepare composite-damaged and acid-etched rock samples with varying acid exposure times, simulating the rock state under perforation fracturing combined with acidification for enhanced permeability. Uniaxial compression tests, XRD experiments, and SEM analyses were conducted on the shale samples under different damage states. SEM images underwent binarization, and together with low-temperature nitrogen adsorption tests, the influences of different damage treatments on the mechanical properties, energy dissipation, micro-morphology, and pore characteristics of the rock samples were systematically studied. The main conclusions are as follows:

(1) Synergistic degradation of mechanical properties: Impact damage and acidization exhibit synergistic degradation on shale mechanics. Damage treatments reduce peak stress and elastic modulus while increasing peak strain. Mechanical properties and elastic modulus are inversely proportional to acid-etching time. Combined-damage shales show lower peak stress and elastic modulus than single acid-etched shales at the same time. The mechanical properties of combined-damage sample SA28d are the lowest (147.10 MPa), representing a 43.53% reduction from the Blank group.

(2) Energy dissipation enhancement: The untreated Blank sample has the highest total energy and elastic strain energy. Damage treatments decrease both while increasing the dissipated energy ratio. The dissipated energy ratio is positively correlated with acid-etching time. Combined-damage samples show higher ratios than single acid-etched ones. SA28d has the highest ratio (34.74%), 30.23% higher than Blank (4.51%), indicating that damage treatments increase internal micro-cracks and local damage, with synergistic perforation-acidizing causing more pronounced degradation.

(3) Changes in micro-morphology due to acid etching: Untreated shale features a dense microstructure with tightly embedded white mineral particles and minimal micro-pores. Acidization reduces mineral particle size, increases inter-particle pores and micro-cracks, and fragments the interface. Compared to single acid-etched samples, combined-damage shales have more numerous and denser pores, with a more fragmented overall structure.

(4) Pore structure optimization: Untreated shale has the lowest total porosity, while combined-damage sample SA28d has the highest. Acid-etching decreases the micropore volume ratio and increases mesopore/macropore proportions. Porosity increases with prolonged acid immersion. Composite treatment of impact damage and acidization significantly enhances mesopore/macropore ratios compared to single acidization.

In summary, when employing perforation-acidification technology for shale gas extraction, perforation induces mechanical damage, forming weak structural planes and micro-cracks. Acidization promotes carbonate dissolution and clay mineral hydrolysis, expanding pores/fractures, degrading microstructures, and weakening mechanical properties. Longer acid exposure enhances pore development, fracture connectivity, and mechanical damage, improving fracture network complexity and gas desorption/migration efficiency. For low-permeability/low-porosity shale, it is recommended to adopt a combined operation mode of perforation and acidification (15%) to enhance permeability. Short-term acidization (< 7 d) maintains bearing capacity, while long-term acidization (≥ 14 d) optimizes permeability to enhance shale gas recovery efficiency.

CRediT authorship contribution statement

Mao Jing: Writing – original draft, Formal analysis. **Kang Peng:** Resources, Methodology. **Tao Wu:** Data curation. **Han-Kuo Zhang:** Visualization. **Si-Yu Gao:** Software, Project administration.

Declaration of competing interest

The authors declare that they have no known competing financial interests or personal relationships that could have appeared to influence the work reported in this paper.

References

Adnan, A.H., Mohammad, A.H., Awni, A.O., et al., 2009. Effect of demineralization of El-lajjun Jordanian oil shale on oil yield. Fuel Process. Technol. 90 (6), 818–824. https://doi.org/10.1016/j.fuproc.2009.03.005.S.

Cash, R., Zhu, D., Hill, A.D., 2016. Acid Fracturing Carbonate-Rich Shale: a Feasibility Investigation of Eagle Ford Formation. SPE Asia Pacific Hydraulic Fracturing Conference. https://doi.org/10.2118/181805-MS.

Chang, X., Wang, X.Y., Yang, C.H., et al., 2024. Experimental investigation on mode I fracture characteristics of longmaxi formation shale after cyclic thermal shock and high-temperature acid etching treatments. Eng. Fract. Mech. 295 (23), 109762. https://doi.org/10.1016/j.engfracmech.2023.109762.

Chen, T.Y., Lai, G.M., Cheng, Z.Y., et al., 2019. Experimental study on pore evolution of longmaxi shale under acidification. J. China Coal Soc. 44 (11), 34803490. https://doi.org/10.13225/j.cnki.jccs.2018.1511.
Cheng, G.X., Wu, C.F., Jiang, B., et al., 2024a. Pore structure evolution of organic-rich shale induced by structural deformation based on shale deformation experiments. Energy 306 (15), 132463. https://doi.org/10.1016/j.energy.2024.132463.
Cheng, H.R., Wei, J.G., Zhou, X.F., et al., 2024b. Experimental study on the effect of microscale wettability of shale to chemical agents by using nuclear magnetic resonance method. Powder Technol. 445 (1), 120084. https://doi.org/10.1016/j.powtec.2024.120084.
Grieser, W.V., Wheaton, W.E., Magness, W.D., et al., 2007. Surface reactive fluid's effect on shale. Production and Operations Symposium. https://doi.org/10.2118/106815-MS.
Hu, S.C., Zhang, C.X., Ru, W.K., et al., 2023. Creep properties and energy evolution characteristics of weakly cemented rock under step loading. Int. J. Rock Mech. Min. Sci. 170, 105428. https://doi.org/10.1016/j.ijrmms.2023.105428.
Huang, F.S., Wang, F.B., Chen, F., et al., 2024a. Transport and retention of coal fines in proppant packs during gas-water two-phase flow: insights from interface, pore, to laboratory scales. Energy Fuel. 38 (14), 1267212683. https://doi.org/10.1021/acs.energyfuels.4c02255.
Huang, F.S., Wang, F.B., Sang, S.X., et al., 2024b. Effect of flow velocity on clogging induced by coal fines in saturated proppant packs: a transition from surface deposition to bridging. ACS Omega 9 (29), 3206632079. https://doi.org/10.1021/acsomega.4c04121.
Jing, M., Ni, G., Xu, Y., et al., 2022. Modeling and optimization of mechanical properties of drilling sealing materials based on response surface method. J. Clean. Prod. 377 (1), 134452. https://doi.org/10.1016/j.jclepro.2022.134452.
Jing, M., Ni, G.H., Zhu, C.J., et al., 2023. Effect of new modified materials on the microscopic pore structure and hydration characteristics of sealing materials in coal seam boreholes. Constr. Build. Mater. 377 (9), 131076. https://doi.org/10.1016/j.conbuildmat.2023.131076.
Li, J., Huang, Q.M., Wang, G., et al., 2022. Experimental study of effect of slickwater fracturingon coal pore structure and methane adsorption. Energy 239 (15), 122421. https://doi.org/10.1016/j.energy.2021.122421.
Li, P., Shen, B.J., Liu, Y.L., et al., 2025a. The fractal characteristics of the pore throat structure of tight sandstone and its influence on oil content: a case study of the chang 7 member of the Ordos Basin, China. Pet. Sci. 22 (6), 19958226. https://doi.org/10.1016/j.petsci.2025.03.016.
Li, Y., Zhang, L., Liu, D., et al., 2025b. Application of micro-CT and digital volume correlation for investigating the macro-/mesoscopic failure mechanism of shale under uniaxial loading: insights into fracture behavior relevant to shale gas recovery. Bull. Eng. Geol. Environ. 84 (2), 82. https://doi.org/10.1007/S10064-025-04101-9.
Li, Z., Ni, G.H., Sun, L.L., et al., 2020. Effect of ionic liquid treatment on pore structure and fractal characteristics of low rank coal. Fuel 262 (15), 116513. https://doi.org/10.1016/j.fuel.2019.116513.
Liu, K.D., Zhou, Y., Zhang, X.P., et al., 2024a. Study on mechanical properties and acoustic emission characteristics of deep diorite under uniaxial compression. Heliyon 10 (2), 24482. https://doi.org/10.1016/j.heliyon.2024.e24482.
Liu, Y.S., Liu, W., Wang, C., et al., 2024b. Mechanical properties and energy evolution of red sandstone under the influence of acid corrosion. Arabian J. Sci. Eng. 49, 1404114054. https://doi.org/10.1007/s13369-024-08886-x.
Luo, S., Gong, F.Q., Li, L.L., et al., 2023. Linear energy storage and dissipation laws and damage evolution characteristics of rock under triaxial cyclic compression with different confining pressures. Trans. Nonferrous Metals Soc. China 33 (7), 21682182. https://doi.org/10.1016/s1003-6326(23)66251-x.
Ma, R.S., Zhang, J.Y., Feng, Q.H., et al., 2024. Effect of cyclic hydraulic stimulation on pore structure and methane sorption characteristics of anthracite coal: a case study in the Qinshui Basin, China. Pet. Sci. 20 (5), 32713287. https://doi.org/10.1016/j.petsci.2024.08.001.
Morsy, S., Hetherington, C.J., Sheng, J.J., 2013. Effect of low-concentration HCl on the mineralogical, mechanical, and physical properties of shale rocks. SPE Eastern Regional Meeting. https://doi.org/10.2118/165689-MS.
Ni, G.H., Fu, Z.L., Li, Z., et al., 2024. Performance study of new lightweight cementitious composites with glass beads as filler. J. Build. Eng. 90, 109477. https://doi.org/10.1016/j.jobe.2024.109477.
Ozoji, T.M., Zhang, Z.X., Aladejare, A.E., et al., 2024. Effect of strain rate on specific fracture energy and micro-fracture surface properties of rock specimen under dynamic uniaxial compression. Eng. Fract. Mech. 295, 109763. https://doi.org/10.1016/j.engfracmech.2023.109763.
Peng, K., Liu, X., Jing, M., et al., 2025. Impact-water interaction effects on mechanical and energy characteristics of granite during uniaxial compression. Geoenergy Sci. Eng. 254, 214033. https://doi.org/10.1016/j.geoen.2025.214033.
Peng, K., Wu, T., Wang, Y.M., et al., 2024. Mechanical behavior and energy characteristics of red sandstone with different seawater immersion heights under biaxial compression. Phys 36 (8), 086620. https://doi.org/10.1063/5.0221591.
Ru, W.K., Hu, S.C., Li, D.Y., et al., 2024. Energy evolution of unloading confining pressure and dissipative energy damage constitutive model of coal-rock combination. Rock Soil Mech. 44 (12), 34483458. https://doi.org/10.16285/j.rsm.2022.1883.
Sheng, M., Khan, W.A., Cheng, S.Z., et al., 2021. J. Nat. Gas Sci. Eng. 88, 103855. https://doi.org/10.1016/j.jngse.2021.103855.
Tan, P., Jin, Y., Han, L., et al., 2018. Mechanism of acid pretreatment on fracturing of deep fractured shale reservoirs. Chin. J. Geotech. Eng. 2, 384390. https://doi.org/10.11779/CJGE201802021 (in Chinese).
Teklu, T.W., Abass, H.H., Hanashmooni, R., et al., 2017. Experimental investigation of acid imbibition on matrix and fractured carbonate rich shales. J. Nat. Gas Sci. 45, 706725. https://doi.org/10.1016/j.jngse.2017.06.001.
Tian, X., Duan, X.G., Sun, M.D., et al., 2024. Evolution of fractal characteristics in shales with increasing thermal maturity: evidence from neutron scattering, N_2 physisorption, and FE-SEM imaging. Energy 298 (7), 131342. https://doi.org/10.1016/j.energy.2024.131342.
Wang, L., Liu, M.X., Zhao, Y.C., et al., 2023. Multi-scale pore structure transformation of shale under mixed acid acidification method. Arab. J. Chem. 16 (8), 104937. https://doi.org/10.1016/j.arabjc.2023.104937.
Wang, Y.F., Wang, J., Liu, H.Q., et al., 2024. Effects of acid–rock reaction on physical properties during CO_2-rich industrial waste gas (CO_2-rich IWG) injection in shale reservoirs. Pet. Sci. 21 (1), 272285. https://doi.org/10.1016/j.petsci.2023.09.016.
Wang, Z.Y., Cheng, Y.P., Wang, G., et al., 2022. Comparative analysis of pore structure parameters of coal by using low pressure argon and nitrogen adsorption. Fuel 309, 122120. https://doi.org/10.1016/j.fuel.2021.122120.
Wei, J., Duan, H.M., Yan, Q., et al., 2021. Shale gas: will it become a new type of clean energy in China? - a perspective of development potential. J. Clean. Prod. 294, 126257. https://doi.org/10.1016/j.jclepro.2021.126257.
Wen, Y.Z., Ni, G.H., Zhang, X.Y., et al., 2023. Fine characterization of pore structure of acidified anthracite based on liquid intrusion method and Micro-CT. Energy 263, 125639. https://doi.org/10.1016/j.energy.2022.125639.
Xiao, Y.J., Yue, W.H., Wu, C.L., et al., 2024. Synergistic effect of oxidation dissolution and acid fracturing in improving shale gas production capacity. Chem. Technol. Fuels Oils 60 (2), 334343. https://doi.org/10.1007/S10553-024-01688-9.
Xu, Y.Y., Arya, L., Rooney, C., et al., 2024. Influence of fracturing fluids on shale matrix permeability and micro-mechanical properties after chemical interactions. Geoenergy Sci. Eng. 241, 213197. https://doi.org/10.1016/j.geoen.2024.213197.
Yu, Y., Wang, Z.H., Tang, C.X., et al., 2023. Energy evolution and fractal characteristics of acid-eroded granite under uniaxial compression. Rock Soil Mech. 44 (7), 19711982. https://doi.org/10.16285/j.rsm.2022.1204 (in Chinese).
Zhang, H., Zhang, Y., Liu, W., et al., 2023. The influence of acid on the rock mechanical characteristics of deep shale in the Wujiaping formation. Energy Eng 121 (1), 2742. https://doi.org/10.32604/ee.2023.041410.
Zhang, S.S., Liu, H., Wu, C.F., et al., 2022. Influence of particle size on pore structure and multifractal characteristics in coal using low-pressure gas adsorption. J. Pet. Sci. Eng. 212, 110273. https://doi.org/10.1016/j.petrol.2022.110273.
Zhao, C.X., Liu, J.F., Dai, H.Y., et al., 2024. Frictional evolution process and stability properties of longmaxi shale under fluid injection. Energy 294, 130910. https://doi.org/10.1016/j.energy.2024.130SS910.